# Quantification of Lipoprotein Uptake *in Vivo* Using Magnetic Particle Imaging and Spectroscopy

*Staffan Hildebrand[†], Norbert Löwa[‡], Hendrik Paysen[‡], Raluca M. Fratila[§,¶], Laia Reverte Salisa[†], Thithawat Trakoolwilaiwan[‖,⊥], Zheming Niu[†], Georgios Kasparis[‖,⊥], Stephanie Franziska Preuss[†], Olaf Kosch[‡], Jesus M. de la Fuente[§,¶], Nguyen Thi Kim Thanh[‖,⊥], Frank Wiekhorst[‡], Alexander Pfeifer[†]\**

[†] Institut für Pharmakologie und Toxikologie, Rheinische Friedrich-Wilhelms-Universität Bonn, Sigmund-Freud-Str. 25, 53127 Bonn, Germany

[‡] 8.23 Metrology for Magnetic Nanoparticles, Physikalisch-Technische Bundesanstalt, Abbestraße 2–12, 10587 Berlin, Germany

[§] INMA – Instituto de Nanociencia de Materiales de Aragón, Campus Rio Ebro, Edificio I+D, C/ Mariano Esquillor s/n, 50018 Zaragoza, Spain

[¶] Centro de Investigación Biomédica en Red de Bioingeniería, Biomateriales y Nanomedicina (CIBER-BBN), 28029 Madrid, Spain

[‖] Biophysics Group, Department of Physics and Astronomy, University College London, Gower Street, London WC1E 6BT, UK

[⊥] UCL Healthcare Biomagnetics Laboratories, University College London, 21 Albemarle Street, London W1S 4BS, UK

\* alexander.pfeifer@uni-bonn.de

ABSTRACT

Lipids are a major source of energy for most tissues, and lipid uptake and storage is therefore crucial for energy homeostasis. So far, quantification of lipid uptake *in vivo* has primarily relied on radioactive isotope labeling, exposing human subjects or experimental animals to ionizing radiation. Here, we describe the quantification of *in vivo* uptake of chylomicrons, the primary carriers of dietary lipids, in metabolically active tissues using magnetic particle imaging (MPI) and magnetic particle spectroscopy (MPS). We show that loading artificial chylomicrons (ACM) with iron oxide nanoparticles (IONPs) enables rapid and highly sensitive *post hoc* detection of lipid uptake *in situ* using MPS. Importantly, by utilizing highly magnetic Zn-doped iron oxide nanoparticles (ZnMNPs), we generated ACM with MPI tracer properties superseding the current gold-standard, Resovist®, enabling quantification of lipid uptake from whole-animal scans. We focused on brown adipose tissue (BAT), which dissipates heat and can consume a large part of nutrient lipids, as a model for tightly regulated and inducible lipid uptake. High BAT activity in humans correlates with leanness and improved cardiometabolic health. However, the lack of non-radioactive imaging techniques is an important hurdle for the development of BAT-centered therapies for metabolic diseases such as obesity and type 2 diabetes. Comparison of MPI measurements with iron quantification by inductively coupled plasma mass spectrometry (ICP-MS) revealed that MPI rivals the performance of this highly sensitive technique. Our results represent radioactivity-free quantification of lipid uptake in metabolically active tissues like BAT.

KEYWORDS

magnetic particle imaging, brown adipose tissue, BAT, chylomicron, TRL, magnetic particle spectroscopy, lipid uptake

Adipose tissues are the major sites of lipid storage. There are two major types of adipose tissue, white adipose tissue (WAT) and BAT. [1] BAT is an organ that is capable of converting chemical energy into heat by mitochondrial uncoupling. [2,3] Since the discovery of metabolically active BAT in adult humans in 2007/9, [4-8] it has been the subject of intense research due to the possibility of exploiting its thermogenic properties for combating obesity, diabetes, dyslipidemia, and cardiovascular disease. [9-11] During the process of thermogenesis in BAT, there is a dramatic increase in the demand for energy substrates and ca. 50-75% of the food-derived lipids and glucose, respectively, are taken up by activated BAT. [12-16] Consequently, quantification of lipid uptake in BAT is a highly valuable tool both to measure BAT activity, as well as to develop ways to measure lipid transport and storage. Additionally, safe and non-invasive measurements of BAT activity in humans would be an important prerequisite for the development of anti-obesity drugs.

Lipoprotein particles are composed of triglycerides, phospholipids, and cholesterol, and are associated with apolipoproteins (ApoA, ApoB, ApoC, and ApoE), which confer functionality and tissue targeting capabilities. [17,18] Classification of lipoprotein particles is based on particle size and density: high density lipoprotein particles (HDL), low density lipoprotein particles (LDL), intermediate density lipoprotein particles (IDL), and very low density lipoprotein particles (VLDL) range from 5 to 100 nm in diameter, respectively, and take part in lipid transport between the liver and peripheral tissues. Ultra low density lipoprotein particles

(ULDL), also known as triglyceride-rich lipoprotein particles (TRL) or chylomicrons, are between 100 and 1000 nm in diameter and represent the primary means of transport for dietary lipids between the gut and peripheral tissues. [18, 19] Artificial lipoprotein particles have found a variety of uses in research, including analysis of nutrient uptake and lipid metabolism, diagnostics, and immunotherapy. [13, 20, 21] Uptake of chylomicrons in tissues is canonically mediated by lipoprotein lipase at the endothelium, followed by import of the free fatty acids into the tissue. [17, 22, 23] Alternatively, lipoprotein particles can undergo whole-particle internalization and transcytosis through the endothelium. [13] Activated BAT efficiently takes up lipoprotein particles, and the majority of intravenously administered lipoprotein particles are cleared from the serum within minutes. [13]

Currently, the only imaging technique commonly used for detecting nutrient uptake in humans is positron emission tomography–computed tomography (PET-CT), which involves administering a cumulative dose of ionizing radiation of around 30 mSv for a single round of image acquisition. [24] As this poses a significant health risk for involved subjects, techniques for radiation-free BAT activity measurements are urgently needed. Additionally, the tracers used for metabolic PET-CT imaging, typically $[^{18}F]FDG$ for glucose or $[^{18}F]FTHA$ for lipids, both have drawbacks which limits their use for assessing BAT activity. First, obese subjects are typically diabetic and exhibit impaired cold-induced glucose uptake (and thereby $[^{18}F]FDG$), but not fatty acids. [25] Second, it is currently not possible to measure BAT volume directly using $[^{18}F]FTHA$ due to insufficient radioactivity contrast between BAT and WAT. To circumvent these issues, attempts have been made to measure BAT activity with magnetic resonance imaging (MRI). Using dynamic T2*-imaging, signal fluctuations that correlate with whole-body cooling can be detected, but so far this technique has been hampered by low specificity and contrast. [26] MRI has

also been used in experimental animal models to detect iron oxide-loaded chylomicrons for semi-quantitative measurements. [27] Other methods for assessing BAT activity have been investigated, such as hyperpolarized $^{13}$C-MRI imaging to detect metabolite turnover, and contrast ultrasound to detect changes in blood flow (although this is limited to superficial tissues). [28, 29]

Here, we describe quantification of *in vivo* lipid uptake using MPI and MPS. The MPI/MPS signal is derived from the nonlinear magnetization curve of superparamagnetic particles, [30] a phenomenon which does not occur in biological tissues. MPI is an emerging imaging technique that enables not only three-dimensional imaging but also quantification of magnetic nanoparticles (MNPs) *in vivo*. [31, 32] MPI imaging offers several advantages over current clinically used imaging techniques, such as zero signal tissue attenuation, radiation-free tracers, and high spatial and temporal resolution. [32] Unlike MRI, the tracers in MPI are the only source for signal, leading to extremely high contrast. Furthermore, MRI-based measurements of MNPs require a reference scan prior to particle administration, and the sensitivity of MRI-based MNP detection has been reported to be more than 20 times lower compared to MPI. [33] To date, MPI has primarily been used for cell tracking. vascular imaging, and MPI-guided hyperthermia therapy. [34-38] We show that by using tailored ZnMNPs, MNP-loaded chylomicrons enable high-resolution, non-radioactive imaging and quantification of metabolic activity *in vivo* using MPI. As a model for induced, tissue-specific lipid uptake, we use BAT activation by acute cold exposure, and show that MPI detection of internalized MNPs provides an accurate and safe way of detecting alterations in lipid uptake non-invasively. Additionally, we show that the uptake can be quantified *ex vivo* with high sensitivity in any type of tissue with minimal background noise using MPS (zero-dimensional MPI) using relatively inexpensive and commercially available reagents and equipment.

**Results and discussion**

ACM were synthesized by mixing phosphatidylcholine (PC), triglycerides (TG), and cholesterol. To optimize particle size, the TG content was varied resulting in an optimal size distribution between 100 and 1000 nm at a TG to PC mass ratio of 16:1 (Fig. 1a), with a mean hydrodynamic diameter of 387.2 ± 13 nm (Supplementary Fig. 1a). For initial experiments using MPS, we loaded ACM with oleic acid-stabilized iron oxide magnetic nanoparticles (IONPs) with a diameter of 20 nm. Incorporation of IONPs in the triglyceride core only slightly decreased the mean hydrodynamic diameter (338.6 ± 9 nm), with no discernible effect on polydispersity index or Z-potential (Supplementary Fig. 1b-c). Potential size distribution bias of IONP-loaded ACM was investigated by pulling down highly magnetic IONP-ACM with a permanent magnet and measuring the hydrodynamic size of pulled down ACM and the ones in the non-magnetic supernatant. We found that highly magnetic IONP-ACM had a slightly higher mean hydrodynamic diameter, but that both fractions showed size distributions characteristic of chylomicrons (Supplementary Fig. 1d-e). Embedding of the IONPs in the core of the chylomicrons was corroborated by transmission electron cryomicroscopy (cryo-TEM) as well as negative-stain transmission electron microscopy (TEM) and high-angle annular dark-field scanning transmission electron microscopy (HAADF-STEM) (Fig. 1b and Supplementary Fig. 2, respectively). The negative-stain TEM and HAADF-STEM images appear to show particles of slightly larger size than the cryo-TEM and hydrodynamic diameter measurements, possibly due to morphological changes caused by the sample preparation (e.g. "flattening" of the particles during sample drying). Importantly, the cryo-TEM analysis showed that IONPs were inside the ACM and not on the surface, indicating stable loading and low likelihood of nanoparticle shedding. Incorporation in ACM did not alter the static and dynamic properties of the IONPs: the

quasi-static magnetization curves of IONP-loaded ACM indicate that the individual particles are still sufficiently separated, showing no adverse influence of chylomicron synthesis on the magnetization behavior of the IONPs (Fig. 1c). Nevertheless, both samples show a non-saturating magnetization curve at high fields. This linear contribution has been often attributed to surface spin canting in IONPs and is very likely due to a low amount of crystallographic disorder as found in other IONP samples as well. [39-41] Similar results were obtained by dynamic magnetization measurements using MPS, where no significant change in the spectral magnetic signature was measured for individual IONPs compared to IONP-loaded ACM (Fig. 1d).
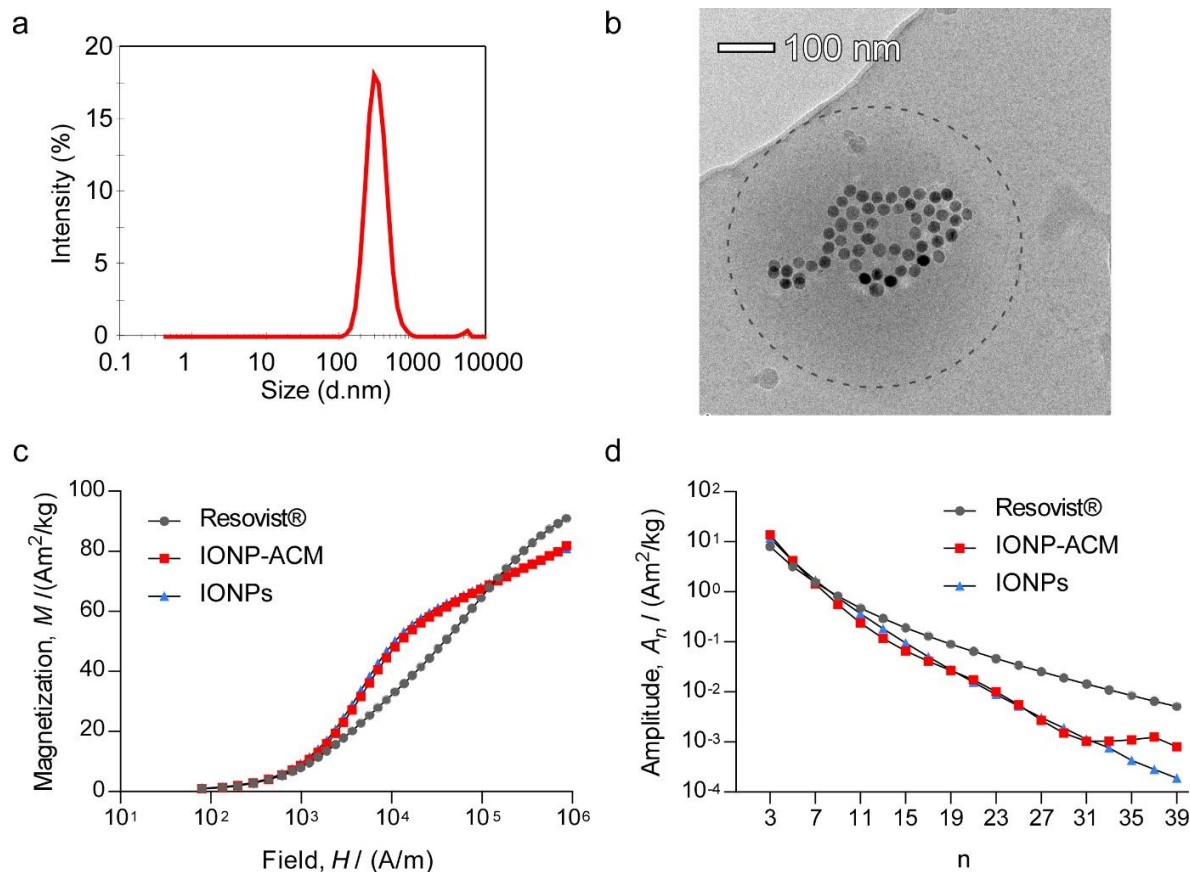


**Figure 1.** Characterization of IONP-ACM. a: Size distribution of IONP-ACM as measured by DLS. b: Representative cryo-TEM image of IONP-loaded ACM. Dashed line outlines the

circumference of the ACM.  c: Quasi-static magnetization curves of three batches of IONP-ACM, with Resovist® and the IONPs used for loading as reference. d: Dynamic magnetization measurements of three batches of IONP-ACM, with Resovist® and the IONPs used for loading as reference; n represents the harmonic number. IONP-ACM data is presented as means ± SEM.

Recent studies have implicated activated BAT as a major site for postprandial TG clearance. [13, 14, 20, 42] Therefore, we used acute cold exposure as a means to induce chylomicron uptake *in vivo*. Cold exposure strongly increases the requirement for intracellular energy substrates to fuel thermogenesis, and therefore induces a rapid influx of glucose and lipids from the circulation. [4, 6, 8, 13] A bolus of 5 ml/kg IONP-ACM was injected in the tail vein of male C57BL/6-J mice following 20 hours of cold (4°C) exposure (Fig. 2a). MPS measurements of tissue lysates revealed a dramatic increase in Fe uptake in the BAT of cold-exposed animals both in terms of Fe uptake per mg of tissue ($0.2 \pm 0.1$ ng/mg (23°C) *vs*. $13.7 \pm 3.2$ ng/mg (4°C), Fig. 2b) and per whole tissue ($13.6 \pm 6.3$ ng (23°C) *vs*. $864.6 \pm 163.1$ ng (4°C), Fig. 2c). Compared to visceral WAT, subcutaneous WAT has a large population of inducible brown adipocytes, also known as beige adipocytes, which contribute to whole body energy homeostasis. [1, 43, 44] In line with this, the subcutaneous inguinal WAT depot (iWAT) of cold-exposed mice exhibited a tendency for increased Fe uptake ($0.09 \pm 0.07$ ng/mg (23°C) *vs*. $1.2 \pm 0.4$ ng/mg (4°C) for specific uptake, p = 0.0708, Fig. 2b, and $23.8 \pm 20.2$ ng (23°C) *vs*. $177.9 \pm 53.4$ ng (4°C) for total uptake, p = 0.0541, Fig. 2c). In contrast, no increase in Fe uptake could be observed in the visceral gonadal WAT depot (gWAT, Fig. 2b-c). Cold exposure also induces shivering of skeletal muscle, increasing its energy substrate requirements. [45, 46] Accordingly, a significant increase in Fe uptake was also

detected in the quadriceps of cold-exposed mice (Fig. 2b). These data demonstrate that ACM uptake in metabolically active tissues is quantifiable by MPS-based measurements.

To evaluate the detection limit of MPS-based measurement of ACM uptake in adipose tissue, we performed a more detailed analysis focusing on minor BAT depots as well as depots of beige fat. Perirenal BAT (pBAT) is a small depot of BAT adjacent to the kidneys. The perivascular adipose tissue (PVAT) surrounding the thoracic aorta is another small fat depot that has been reported to resemble BAT in several studies. [47, 48] Fe uptake in pBAT and PVAT was increased in cold exposed animals to 10-fold and 12.2-fold, respectively (Fig. 2d). Thus, Fe uptake in the small BAT depots (pBAT and PVAT) was detected by MPS and amounted to similar increases as "classical" interscapular BAT upon cold exposure (Fig. 2d). To evaluate ACM uptake in beige adipocytes, we compared visceral WAT, which typically has low numbers of beige adipocytes, to subcutaneous WAT, which more readily undergoes "beiging" upon cold exposure and has a high number of beige adipocytes. Visceral WAT, *i.e.* gWAT, mesenteric WAT (mWAT), and retroperitoneal WAT (rWAT), did not show any increase in Fe uptake after short-term cold exposure. On the other hand, the subcutaneous adipose tissue depot triceps-associated WAT (triWAT), showed a tendency for increased Fe uptake (p = 0.056, Fig. 2e, Supplementary Fig. 3), and the subcutaneous interscapular WAT (isWAT) depot showed significantly more Fe content after cold exposure (Fig. 2e, Supplementary Fig. 3). Prolonged cold exposure is well described to induce a strong beige phenotype in WAT [1-3]. Therefore, to induce a more robust beiging of the WAT, we also exposed mice to one week of 4°C and injected IONP-ACM. We analyzed Fe uptake in all major WAT depots using MPS, and found a significant increase in all measured depots (Supplementary Fig. 4). This shows that MPS-based quantification of IONP-ACM uptake can be used to measure beiging of WAT. Interestingly, this also indicates that activated beige fat

clears chylomicrons from the circulation at least partly by whole-particle uptake. Importantly, these findings demonstrate that MPS-based quantification of lipid uptake has sufficient sensitivity to detect increased lipid uptake in even the smallest BAT depots, as well as in different depots of beige fat. The limit of detection (LOD) for the third harmonic amplitude $A_3$ based MPS-quantification was determined to be 2.1 ng Fe (Supplementary Fig. 5). This enabled accurate quantification of lipid uptake in BAT samples as small as 3 mg even in mice housed at room temperature. Interestingly, the magnetization curve of IONP showed clearly linear correlation at higher field values, meaning that the spin canting is predominant for this commercial type of particles. Therefore, only a reduced part of the nanoparticular iron will contribute to the MPS signal. Thus, using particles with higher crystallographic order may result in stronger signals and lower detection limits.
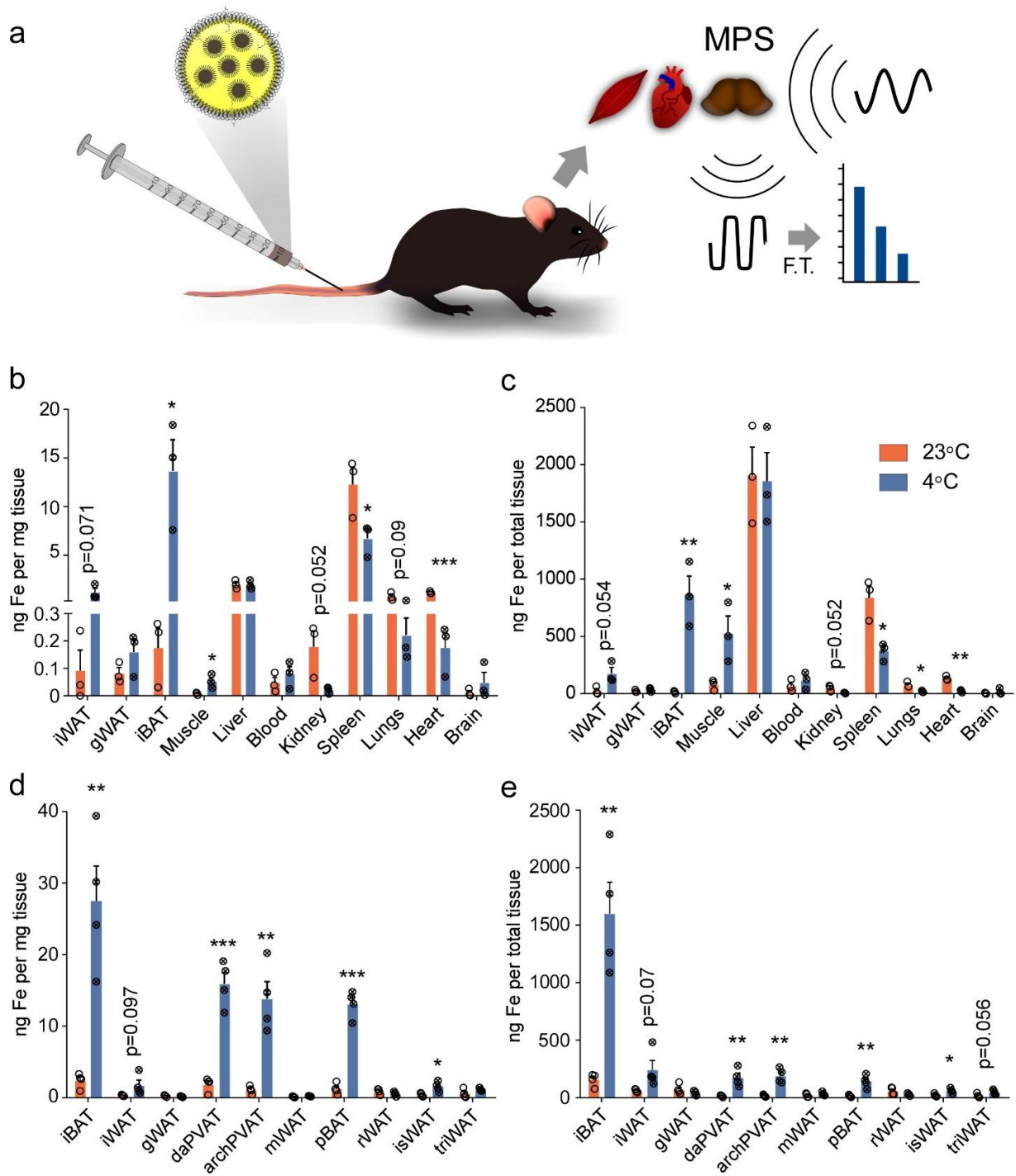
**Figure 2.** MPS-based quantification of IONP-ACM uptake in tissues after cold exposure. a, Schematic representation of the experimental setup. F.T.: Fourier transform. b,c: Specific and total uptake of IONP-ACM in different organs after 20 hours cold-exposure (n=3 mice per

group). d,e: Specific and total uptake of IONP-ACM in BAT and WAT depots after 20 hours cold-exposure (n=4 mice per group). iBAT: Interscapular BAT, daPVAT: Descending aorta PVAT, archPVAT: Aortic arch PVAT. Data is presented as means $\pm$ SEM, * = $p < 0.05$, ** = $p < 0.01$, *** = $p < 0.001$, two-tailed student's t-test, 23°C *vs* 4°C.

To verify that the incorporated IONPs enter brown adipocytes, the mature adipocytes from various adipose tissue depots were separated from the stromal vascular fraction (SVF) containing preadipocytes, endothelial cells, and other non-adipocytes. In both BAT and iWAT, Fe uptake was significantly increased in the mature adipocyte fraction compared to the SVF fraction upon cold exposure ($5.5 \pm 1.0$-fold and $1.8 \pm 0.1$-fold, respectively (Fig. 3a-b), but not in animals kept at ambient temperature. In gWAT, no significant difference in Fe uptake between mature adipocytes and SVF could be observed (Fig. 3c). Additionally, TEM and STEM images of BAT samples from cold-exposed, IONP-ACM injected mice showed both IONP-ACM apparently undergoing endocytosis in the endothelium, as well as deposition of the IONPs specifically in brown adipocytes (Fig. 3d and Supplementary Fig. 6). The latter was confirmed by Energy-dispersive X-ray spectroscopy (EDX) analysis of BAT tissue sections (Supplementary Fig. 7). IONP deposition in the BAT of cold-exposed mice was also confirmed with Prussian Blue staining, which showed bright blue signal in the BAT of mice exposed to 4°C, but not in those exposed to 23°C (Fig. 3e). Therefore, we conclude that Fe-content as measured by MPS and MPI after IONP-ACM injection represents true chylomicron uptake in BAT.
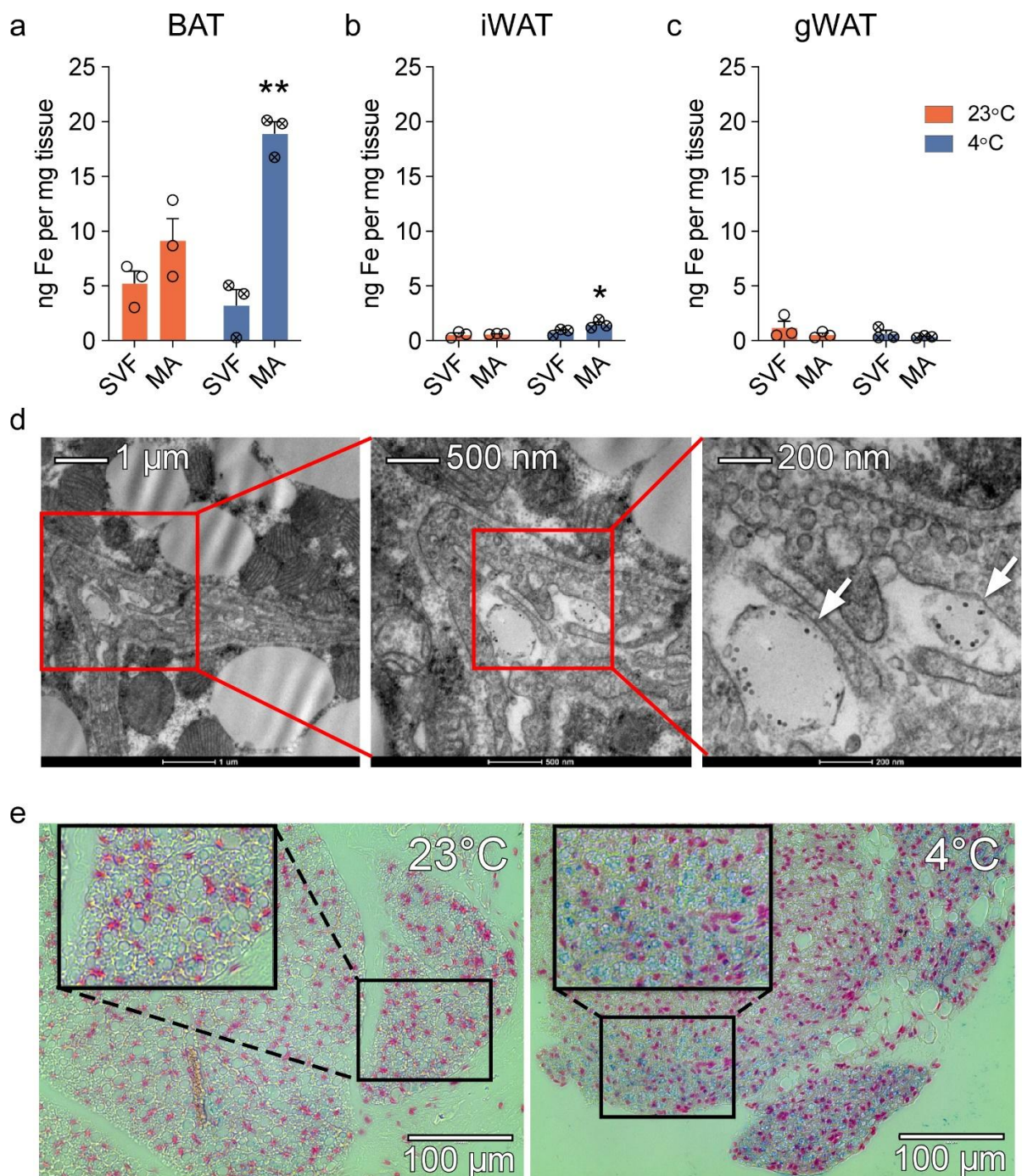
**Figure 3.** IONP-ACM are specifically taken up by the brown adipocytes in BAT. a-c: Fe uptake in SVF and MA in BAT, iWAT, and gWAT after exposure to either 23°C or 4°C (n=3 mice per group). d: TEM images showing uptake of IONP-ACM (arrows) in the capillaries of BAT. e:

Representative images of Prussian Blue/Pararosaniline-stained BAT from mice injected with IONP-ACM after exposure to 23°C or 4°C. Data is presented as means ± SEM. * = p < 0.05, two-tailed student's t-test, SVF *vs.* MA.

To examine the feasibility of using MPI together with the MNP-loaded ACM for measuring lipid uptake and metabolic activity *in vivo*, the suitability of ACM as MPI tracers was assessed. The harmonic spectra of the IONP-ACM used in the experiments above showed low amplitudes in the higher harmonics compared to Resovist®, and were thus considered inadequate for MPI. To improve the harmonic spectra of the ACM and thus MPI signal, we focused on incorporating nanoparticles with higher magnetic saturation. Zn-doping of iron oxide nanoparticles has previously been shown to increase saturation magnetization. [49] Therefore, we focused on Zn-doped MNPs (ZnMNPs) and incorporated these into ACM. The ZnMNPs used here had a mean diameter of 10 ± 2 nm (as measured by TEM) and a saturation magnetization of 110 emu/g. The resulting ZnMNP-ACM showed high signal amplitudes and a rich harmonic spectrum comparable to that of Resovist® (Fig. 4a). As the signal amplitudes in the harmonic spectrum strongly depend on the magnetization properties of the particles, we also compared the magnetization curves of Resovist® with that of the ZnMNP-ACM. This showed that the ZnMNP-ACM had a considerably higher saturation magnetization than Resovist® (Fig. 4b). This indicates that, unlike IONP-ACM, the magnetic properties of ZnMNP-ACM make them well suited for MPI applications. The ZnMNP-ACM had a mean diameter of 309.3 ± 13.2 nm (Supplementary Fig. 8a), with a similar size distribution as the IONP-ACM (Supplementary Fig. 8b). Incorporation of ZnMNPs in the ACM was confirmed by HAADF-STEM and EDX (Supplementary Fig. 8c).

A systematic MPS evaluation of the ZnMNP-ACM as MPI tracer was then performed with Resovist® as reference. Importantly, serial dilution of ZnMNP-ACM showed that the MPS spectrum of ZnMNP-ACM scales linearly with concentration (Fig. 4c-d), which is necessary for quantitative MPI. Additionally, encapsulation of the ZnMNPs in ACM rendered their magnetic properties extremely insensitive to the surrounding environment, unlike the current gold-standard tracer for MPI, Resovist® (Fig. 4e). To compare the spatial resolution performance of Resovist® and ZnMNP-ACM, we also measured the full width at half maximum (FWHM) of point-like phantoms, which showed slightly increased FWHM for ZnMNP-ACM (Supplementary Fig. 9). These data indicate that ZnMNP-ACM are well suited for use as MPI tracers.
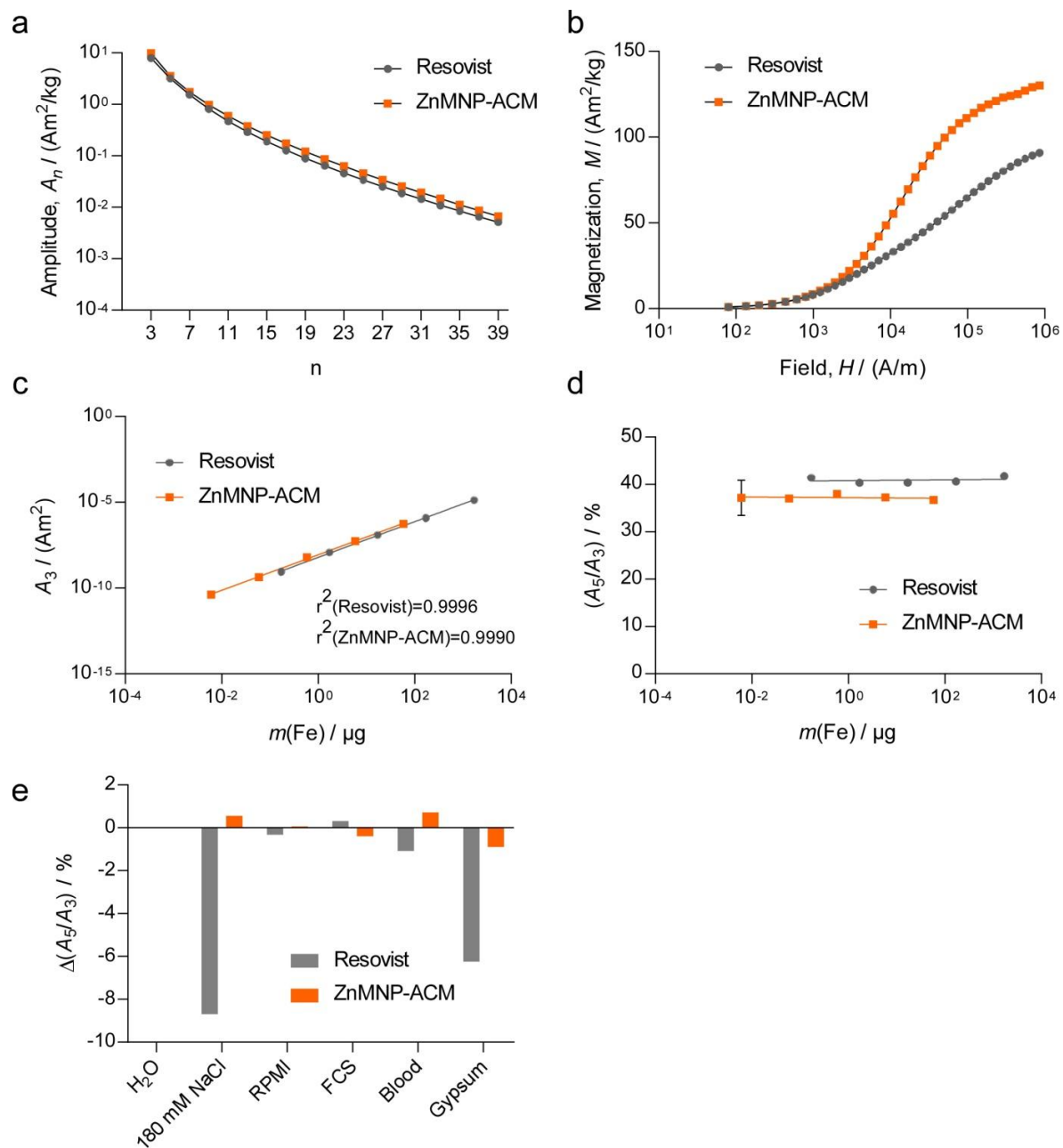
**Figure 4.** MPS-based evaluation of ZnMNP-ACM as MPI tracer. a: MPS amplitude spectrum of ZnMNP-ACM and Resovist®. b: Magnetization curves of ZnMNP-ACM and Resovist®. c: MPS signal amplitude after serial dilution parametrized by A3. d: MPS spectrum shape after serial dilution parameterized by the harmonic ratio A5/A3. e: Change of MPS signal shape

(A5/A3) in different biological environments. Data is presented as means ± SD of 20 repeated measurements. RPMI: Roswell Park Memorial Institute medium, FCS: Fetal calf serum.

To demonstrate the performance of ZnMNP-ACM as MPI tracers, ZnMNP-ACM were administered to mice which were then analyzed by whole-animal MPI scans (see Supplementary Fig. 10 for workflow). As shown in Fig. 5, MPI enabled clear visualization of lipid uptake in active BAT. For comparison, control mice were injected with Resovist® with or without prior cold exposure. In contrast to ZnMNP-ACM-injected mice, no MPI signal could be detected in the interscapular area of Resovist®-injected mice (Fig. 5b). MPS-based quantification of Resovist® uptake in isolated organs showed no uptake in BAT, iWAT, or gWAT (Supplementary Fig. 11). Quantification of ZnMNP content in the interscapular area of mice injected with ZnMNP-ACM showed a significant increase upon cold exposure (8.7 ± 1.0-fold, Fig. 5c-d).
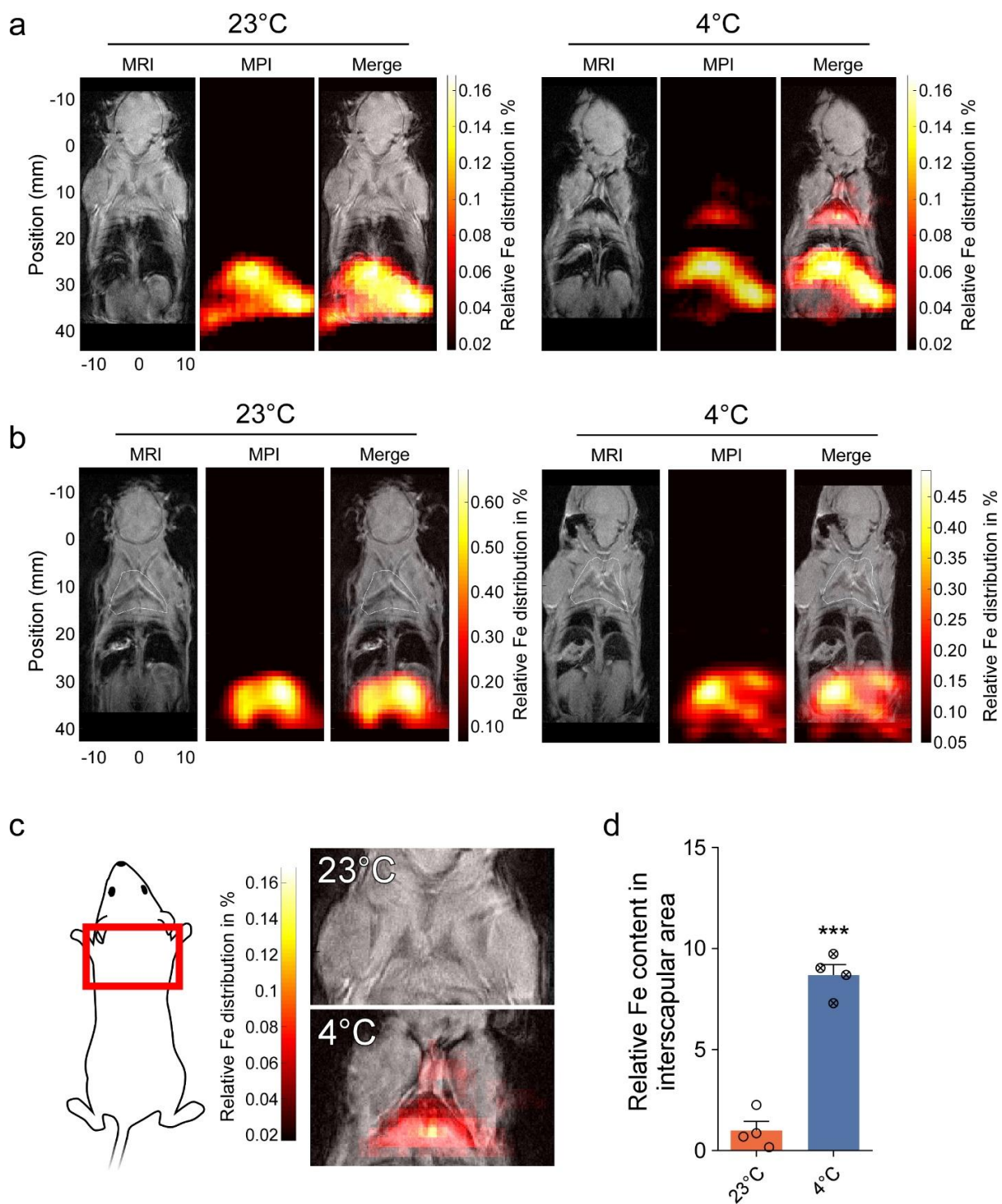
**Figure 5.** MPI-based quantification of ZnMNP-ACM uptake in BAT after cold exposure. a: Representative whole-body MRI and MPI images of mice injected with ZnMNP-ACM after

exposure to either 23 °C or 4 °C. b: Representative whole-body MRI and MPI images of mice injected with Resovist® after exposure to either 23 °C or 4 °C. c: Representative MPI images of the interscapular area (red box) with MRI overlay. d: ZnMNP-ACM uptake in BAT after 20 hours cold-exposure measured from whole-animal MPI scans (n=4 mice per group). Data is presented as means ± SEM relative to uptake at 23°C in each tissue, ** = p < 0.01, *** = p < 0.001, two-tailed student's t-test, 23°C *vs*. 4°C.

After measuring tissue uptake of ZnMNP-ACM by whole-body MPI scans, tissues were extracted from the mice and Fe content quantified again *ex vivo* using both MPI (Fig. 6a-c) and MPS. MPI quantification of the Fe content in extracted BAT showed a similar increase in Fe content as the whole-body scans (10.4 ± 1.5-fold, Fig. 6b). The imaging of individual organs also confirmed that no signal was emanating from organs proximal to the BAT, such as the lungs or heart (Fig. 6c). Although we saw a tendency for increased uptake in iWAT in our MPS measurements, we were not able to detect any differences with MPI (Fig. 6c), possibly due to slightly lower sensitivity when compared to *ex vivo* MPS. We did not detect any differences in BAT uptake between mice housed at 23°C compared to mice housed in thermoneutral conditions (30°C, Supplementary Fig. 12). This in good agreement with data on radioactively labeled artificial chylomicrons, which are taken up by BAT through whole-particle endocytosis mainly upon cold exposure. [14] The results from MPI- and MPS-based measurement of ZnMNP content correlated strongly ($r^2$>0.99) underlining that the selected algorithm and the parameters for image reconstruction do not adversely affect the quantitative information contained in the raw data of the MPI measurement (Supplementary Fig. 13).
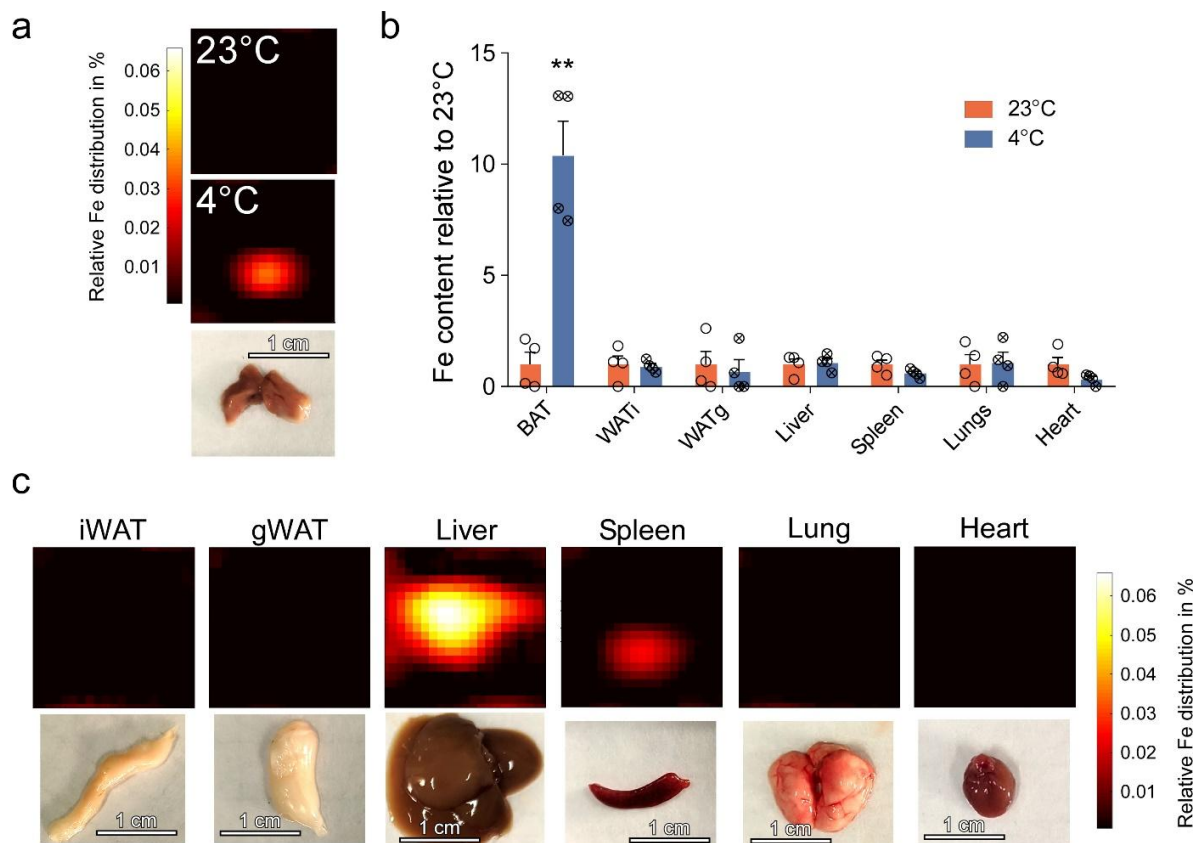
**Figure 6.** MPI-based quantification of ZnMNP-ACM uptake in isolated organs after cold exposure a: Representative MPI images of excised BAT, with representative photograph of BAT at the same scale. b: ZnMNP-ACM uptake in excised tissues after 20 hours cold-exposure measured from single-organ MPI scans (n=4 mice per group). Data is shown as fold-change over Fe content in each organ of the mice housed at 23°C. c: Representative MPI images of isolated organs from cold-exposed mice injected with ZnMNP-ACM. Representative photographs of the organs imaged is shown below each MPI image. Data is presented as means ± SEM relative to uptake at 23°C in each tissue, ** = p < 0.01, *** = p < 0.001, two-tailed student's t-test, 23°C *vs.* 4°C.

As the injected ACM to a large extent end up in the liver, we performed a long-term elimination study to investigate hepatic clearance of the ZnMNP-ACM. This showed a significant decrease of MNP content over time, with less than 20% of the MPS signal remaining after 4 weeks (Supplementary Fig. 14). To verify that the ZnMNP-ACM uptake measured by MPI is indeed due to uptake of Zn-MNP-loaded ACM and not free ZnMNPs, we also injected cold-exposed and control mice with free ZnMNPs. We could not detect any uptake of ZnMNPs in BAT using MPS in either group, suggesting that our MPI results represent *bona fide* ACM uptake (Supplementary Fig. 15). Although both zinc and iron are widely considered to be biocompatible materials with minimal safety concerns in the concentration range used in this study, [50, 51] we also investigated the effect of both ZnMNP-ACM and Resovist® on brown adipocytes *in vitro*. We could not detect any significant effect of the nanoparticles on brown fat differentiation, cellular toxicity, or inflammatory cytokine expression (Supplementary Fig. 16-17). The *in vivo* toxicity of zinc-doped iron oxide nanoparticles has been studied after intragastric administration, with no observed adverse effects [52]. Additionally, intravenous administration of zinc oxide nanoparticles led to adverse effects in rats starting at 5 mg/kg [53]. The zinc content in the MNPs used in this study is ~6.5 times lower than the iron content. This results in a zinc dose of approximately 300 µg/kg for the ZnMNP-ACM-injected mice, more than 15 times less than previously observed toxic doses of zinc oxide nanoparticles. Therefore, we do not expect the zinc doping to be a limiting factor in terms of toxicity of the ZnMNP-ACM.

Finally, to validate the quantitative performance of our MPI measurements, we compared our results with ICP-MS measurements of the same tissue samples. This showed a relatively small ($1.46 \pm 0.15$-fold) but significant increase in Fe concentration in BAT from cold-exposed mice (Fig. 7a), and a similar increase ($1.52 \pm 0.23$-fold, $p = 0.0644$) in Zn concentration (Fig. 7b). The

concentrations of iron and zinc in cold exposed mice were still within the physiological ranges, indicating low risk for toxicity. Liver and spleen Fe and Zn concentrations were also both within physiological ranges (Fig. 7a-b). [54, 55] Comparison of our MPI-based (magnetic) Fe uptake measurements on the ppm scale revealed that the increased concentration of Fe in BAT after cold exposure is not significantly different when measured by MPI or ICP-MS (Fig. 7c, Supplementary Fig. 18). This shows that MPI-based measurement of Fe uptake in BAT is comparable in sensitivity to ICP-MS, albeit with much higher specificity due to the fact that MPI measures only magnetic iron, and not endogenous iron present in the tissues. Importantly, these data show that quantification of ZnMNP-ACM-derived iron using MPI is comparable in performance with the current gold standard in iron quantification in tissue lysates.

The main limitation of the MPI-based quantification of lipid uptake observed in this study was related to the small field of view (FOV) of current preclinical MPI scanners. Using the highest gradient strength to achieve a highly spatially resolved image, the FOV is limited to around $2x2x1$ cm$^3$. A multi-patch acquisition scheme was used to increase the total FOV, but due to signals generated from nanoparticles outside the FOV, imaging artifacts at the edges of each individual reconstruction were present. While we partly corrected for this by "overscanning" the field-free point trajectory [56] to remove imaging artifacts from outside the FOV, we believe that these problems can be resolved better by a different system function acquisition scheme using focus fields. [57] While the resolution achieved using ZnMNP-ACM was sufficient to accurately resolve BAT using MPI, it is likely that improvements could be made by further tracer optimization, as other studies have demonstrated MPI tracers with an even larger relative increase in FWHM compared to Resovist®. [58, 59] Another potential limitation in regards to absolute quantification of iron uptake using MPI is the possibility of nanoparticle aggregation

after uptake, which may affect the MPI signal. Although the ZnMNP-ACM do not show any altered magnetic behavior in different biological environments, we cannot exclude that intracellular processing of the ZnMNP-ACM results in some degree of nanoparticle aggregation. However, since the MPI-based quantification does not yield significantly different results compared to ICP-MS, one would not expect this effect to have a significant impact on the measurements. Given the recent advancement of the development of human MPI scanners, [60] investigating lipid uptake and BAT metabolic activity in human subjects without significant exposure to radiation may be possible.
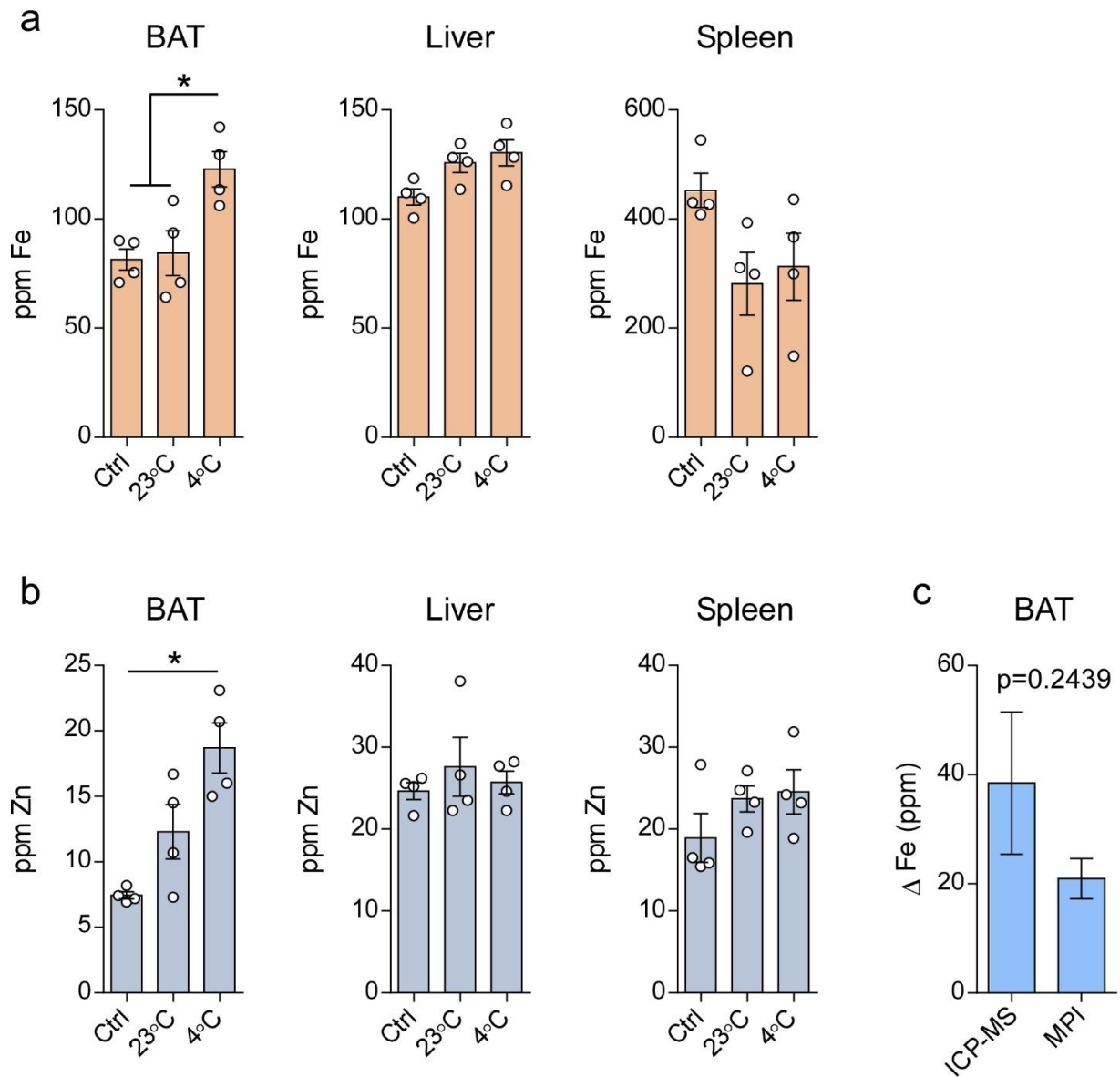
**Figure 7.** ICP-MS-based quantification of ZnMNP-ACM uptake in BAT after cold exposure. a: ICP-MS measurements of Fe concentration in tissue samples from ZnMNP-ACM-injected mice (n=4 mice per group). b: ICP-MS measurements of Zn concentration in tissue samples from ZnMNP-ACM-injected mice. c: comparison between increase in Fe content in BAT upon cold exposure and ZnMNP-ACM injection, as measured by ICP-MS and MPI (n=4 mice per group).

Ctrl: control mice, not injected with ZnMNP-ACM. Data is presented as means ± SEM, * = p < 0.05, two-tailed student's t-test, 23°C *vs.* 4°C or ICP-MS *vs.* MPI.

**Conclusions**

Current strategies for the quantification of *in vivo* lipid uptake rely on radioactive labeling of fatty acids, cholesterol, or other components of the lipoprotein particles. [13, 14, 42, 45, 61-63] While this method has benefits in terms of versatility and by being a *bona fide* measure of lipid uptake, there are clear practical and safety-related drawbacks. Apart from the health concerns inherent in working with radioactive substances, the most common radioisotope for metabolic imaging is $^{18}$F, which has a half-life of 110 minutes – meaning on-site cyclotrons are often required. In this work, we have demonstrated a safe, fast, and highly sensitive technique for measuring chylomicron uptake in metabolically active tissues using IONP-loaded chylomicrons and MPS. Furthermore, we have shown that chylomicrons loaded with strongly magnetic ZnMNPs are highly suitable for MPI imaging, enabling quantification of MNP uptake with similar sensitivity as gold standard *ex vivo* methods like ICP-MS. Taken together, using these tracers, we were able to non-invasively image and quantify chylomicron uptake in metabolically active tissues with great accuracy without relying on radioactive isotope labeling.

METHODS

**Synthesis of artificial MNP-loaded chylomicrons.** Artificial chylomicrons were synthesized by mixing cholesterol (Sigma-Aldrich, St. Louis, USA), phosphatidylcholine (Avanti polar lipids, Alabaster, USA), and triglycerides (soy bean oil, Sigma-Aldrich, St. Louis, USA) in a 1:1:16 ratio, unless otherwise described. The mixture was dissolved chloroform (Sigma-Aldrich, St.

Louis, USA), and 500 µg superparamagnetic iron oxide nanoparticles (Sigma-Aldrich, St. Louis, USA, product nr. 900088) or Zn-doped iron oxide nanoparticles (see below) were added. The mixture was then placed in a rotary evaporator with a heated water bath (60°C) at 75 mbar until all chloroform had evaporated. The resulting lipid film was mixed with 1 ml phosphate buffered saline and sonicated with a probe sonicator at maximum power for 10 minutes with intermittent cooling on ice. Before use, the MNP-ACM suspension was filtered through a 1 µm polyethersulfone (PES) syringe filter (GE Healthcare Life Sciences, Chicago, USA) and immediately characterized using dynamic light scattering (ZetaSizer 90S, Malvern Panalytical, Malvern, UK).

**Zn-doped iron oxide nanoparticles.** The synthesis of zinc ferrite nanocrystals was prepared by incorporating a zinc precursor in a triethylene glycol and iron acetylacetonate mixture as described previously in a high temperature and high pressure reaction. [64]

**ZnMNP surface functionalization.** To render the nanoparticles hydrophobic, oleic acid was used to coat the surface. Briefly, oleic acid (0.5 ml) was dissolved in hexane (5 ml) under magnetic stirring. Then crude nanoparticle suspension (0.5 ml) was added, and the reaction was allowed to proceed overnight at room temperature. The black hexane layer was isolated and washed three times with water to remove triethylene glycol and once with ethanol to remove excess oleic acid. The oleic acid coated nanoparticles were collected by magnetic decantation and redispersed in hexane. The surface coating was assessed by infrared spectroscopy using an ATR-FTIR instrument (Spectrum 100, PerkinElmer) as shown in Supplementary Fig. 19.

**ZnMNP material characterization.** The size and morphology of the crystallites was assessed by TEM by measuring at least 300 particles using the image processing software ImageJ. The

spherical ZnMNPs have an average size of $10 \pm 2$ nm. The magnetic properties were measured on a superconducting quantum interference vibrating sample vibrometer (SQUID-VSM, MPMS 3, Quantum Design, USA).

**Analysis of MNP-ACM uptake *in vivo*.** Wild-type male 8-10 week old C57Bl/6-J mice were purchased from Janvier and randomly divided into two groups (cold exposure or control). The mice were housed at either 23°C or 4°C for 20 hours or one week prior to injection, with free access to chow and water. A bolus of 5 ml/kg of MNP-ACM suspension was injected in the tail vein, immediately followed by an additional 4 hours at either 30°C, 23°C or 4°C, after which the animals were sacrificed. The investigators could not be blinded to the treatment groups due to the obvious differences in temperatures. All animal experiments were approved by the Landesamt für Natur, Umwelt und Verbraucherschutz, Nordrhein-Westfalen, Germany. The governmental approval number is 84-02.04.2016.A171. A total number of 65 mice were used in this study.

*MPS measurements of tissue lysates.* Tissues were extracted with ceramic-coated surgical tools, and digested over night with Proteinase K (Roche, Basel, Switzerland). Digested tissues were homogenized by adding 5-10 glass beads (Sigma-Aldrich, St. Louis, USA) followed by rapid shaking for 20 seconds in CapMix™ (3M ESPE, Seefeld, Germany). 100 µl of the homogenized lysate was transferred to a PCR tube (Applied Biosystems®, Foster City, USA, MicroAmp® fast reaction tube with cap) and measured in the MPS system as described above. For measurements of MNP uptake in different tissue compartments, BAT, iWAT, and gWAT was digested with collagenase, and mature adipocytes were separated from other cells by centrifugation. Prior to quantification a serial dilution of a reference sample was measured by MPS to determine the MNP-specific detection sensitivity from the slope of the calibration curve, *i.e.* the normalized third harmonic amplitude $A_3{}^*=A_3/m(\text{Fe})$. The iron content of the individual tissue sample was

determined from the measured $A_3$ normalized to $A_3$* of the reference. For larger sample sizes a correction of the signal amplitude was necessary taking the spatial dependence of the coil sensitivity into account. [65] To further reduce the quantification uncertainty a subsequent correction of the MNP specific amplitude $A_3$* was performed as previously described for the quantification of MNPs in biological environments and cells. [66, 67]

*MPI measurements.* A preclinical MPI scanner (25/20 FF, Bruker BioSpin, Billerica, USA) was used for all MPI measurements. All MPI measurements were performed post mortem. 3D signal excitation was performed in x/y/z-direction, with slightly different frequencies of ≈24.51/26.04/25.25 kHz and excitation amplitudes of 12 mT. Spatial encoding was achieved by static magnetic gradient fields with gradient strengths of 1.25/1.25/2.5 T/m. Magnetic response signals, generated by the magnetic nanoparticles, were acquired with a gradiometric receive-only coil. [68] The acquired signals were used for image reconstruction of the particle distribution based on the system function approach, [69, 70] after background correction by subtraction of empty scanner measurements and truncation based on the signal-to-noise ratio.

A system function was acquired by measurements of a small reference sample of MNPs at multiple positions all over the field of view (FOV). Due to the small FOV size of MPI, each mouse was measured at four different positions for 10 s (500 averages) and particle distributions were reconstructed individually. The resulting images were joined in one final image covering a FOV of 80x25x19 mm³ with a voxel size of 1 mm³. To remove noise from the final images, a threshold intensity was determined by reconstructions of empty scanner measurements. Detailed lists of all MPI related reconstruction parameters for mice and organs are given in Supplementary Table 1 and 2, respectively. For Fe quantification using MPI data, magnetic iron mass was correlated to voxel intensities based on the system function acquired with a reference

sample with known mass. For color-coding of MPI images, the intensity signal was re-scaled from arbitrary units of voxel intensity to relative Fe distribution in % by setting the sum of all voxel intensities in the images to one.

*MRI measurements.* Anatomical reference scans were acquired using a preclinical 1 T ICON MRI system (Bruker BioSpin, Billerica, USA) equipped with a whole-body receive coil. The same animal bed was used for the MRI and MPI scans without moving the mice between each acquisition. Coronal slices of each mouse were acquired using a FLASH sequence. A detailed list of all MRI related imaging parameters is given in Supplementary Table 3. Image overlay of MRI and MPI images were performed with the help of fiducial markers. Coregistration of the MPI and MRI images were performed the following way: First, MPI measurements of fiducial markers containing MNPs were performed to get reference information which location of the MPI-FOV corresponds to which location on the animal bed. Before the MRI measurements of each mouse, a photo of was taken. An additional fiducial marker, containing only water, was positioned below the animal bed to be able to overlay the MRI image with the photo. Combined with the information obtained from the MPI measurements of the fiducial markers, the MPI and MRI images can be overlaid. For MPI-based uptake quantification in whole-body scans, the ROI (region of interest) for each mouse was selected by identifying the location of the interscapular BAT in the MRI scans, based on the surrounding anatomy.

**Quasi-static magnetic characterization.** The quasi-static magnetization $M$ of the samples as a function of applied field strength  (up to 4000 kA/m) was measured at room temperature using a superconducting quantum interference device (SQUID)-based susceptometer (QD-MPMS-XL-5, Quantum Design, USA). A detailed description of the magnetization measurement procedure is found elsewhere. [71] Here, we used a polycarbonate capsule as a sample container and a clear

straw as a sample holder. The background signal caused by the empty capsule and diamagnetic susceptibility of the dispersion medium was subtracted from the measured signal. The presented magnetization curve results from normalizing the magnetic moment of the sample to its iron content and is given in Am$^2$ per kilogram iron. Therefore, the iron content of the respective sample was determined using a phenanthroline-based iron assay described elsewhere. [72] Measurement data were fitted by the weighted sum of Langevin functions assuming a lognormal distribution of non-interacting magnetic moments. [73]

**Dynamic magnetic characterization.** The dynamic magnetic characterization of MNP was performed by Magnetic Particle Spectroscopy (MPS) using a commercial MPS device (MPS-3, Bruker Biospin, GER). [65] Based on the same physical principle as magnetic particle imaging (MPI), waiving of any spatial encoding, MPS allows for pre-evaluation of the MPI-performance of MNP. For the measurement a PCR tube (Applied Biosystems®, MicroAmp® fast reaction tube with cap) containing a sample volume of up to 100 µL was placed in the MPS system. By exposing the sample to a sinusoidal magnetic field (amplitude $B_p$ up to 25 mT, $f_0$ of 25 kHz) the induced magnetization is measured by gradiometric pick-up coils. Fourier transformation of the measured time signal results spectral components showing distinct amplitudes at odd multiples of the drive frequency $f_0$ evoked by the characteristic non-linear magnetization behavior of MNP. In this study all measurements were performed at 37°C. The limit of detection (LOD) of the third harmonic amplitude $A_3$ was determined according to guidance of the International Union of Pure and Applied Chemistry (IUPAC) as 3x the standard error of the regression y-intercepts (residual standard deviation) in the calibration curve divided by the calibration curve slope.

**Electron microscopy.** The microscopy works have been conducted in the "Laboratorio de Microscopias Avanzadas" at "Instituto de Nanociencia de Aragon - Universidad de Zaragoza".

*Cryo-TEM.* To prepare the sample, a drop of the IONP-ACM suspension was deposited on the carbon side of the copper grid (Electron Microscopy Sciences, Spain) and vitrified by immersion in liquid ethane using an automated device (FEI$^{TM}$ Vitrobot, The Netherlands). All subsequent manipulations of the grid were carried out in liquid nitrogen and the TEM images were acquired under cryogenic conditions using a cryo-transfer holder (Gatan Inc., USA). Images were acquired using a Tecnai T20 microscope (FEI Company, The Netherlands) operating at 200 kV.

*Negative-stain TEM.* For TEM analysis, a carbon coated 300 mesh copper grid was placed on top of a 5 µl droplet of sample (sample facing downwards) for 4 min. The grid was then rinsed on a drop of distilled water and subsequently transferred to a 3 µl drop of NANO-W™ (2% in water; Nanoprobes) for 2 min for negative staining. The grid was quickly rinsed with a drop of water for 1 min to remove the excess of staining solution and dried, contacting the grid edge with filter paper. The grid was stored in an EM grid box under vacuum for future observation by TEM.

*EDX analysis.* For electron microscopy analysis, the excised BAT tissue samples were cut into 1 mm$^3$ pieces and fixed with 2.5% glutaraldehyde/2% paraformaldehyde in 0.1 M pH 7.4 sodium phosphate buffer for 24 h at room temperature and subsequently for 5 days at 4 °C. Following, the samples were washed for 30 min four times with sodium phosphate buffer, postfixed with 2% osmium, rinsed, dehydrated and embedded in Durcupan resin (Fluka, Sigma-Aldrich, St. Louis, USA). Semithin sections (1.5 µm) were cut with an Ultracut UC-6 ultramicrotome (Leica, Heidelberg, Germany) and stained lightly with 1% toluidine blue. Finally, ultrathin sections (0.08 µm) were cut with a diamond knife, stained with lead citrate (Reynolds solution), and examined under a 300 kV transmission electron microscope FEI Tecnai F30 (FEI Company, The Netherlands) equipped with a high angle annular dark field (HAADF) detector and enabling

working in scanning transmission (STEM) mode for performing energy-dispersive X-ray spectroscopy (EDX) analysis.

**Brown adipocyte culture and differentiation.** Brown preadipocytes were isolated, differentiated, and stained with RedO-oil as previously described. [74]

**Prussian blue staining**. Tissue samples were fixed in 4% PFA for 16 h, dehydrated, and embedded in paraffin. 5 μm sections were cut and stained with iron stain kit HT20-1KT (Sigma-Aldrich, St. Louis, USA) according to manufacturer's instructions.

**ATP assay.** ATP analysis was performed with ATPlite Luminescence Assay System (PerkinElmer, Waltham, USA) according to manufacturer's instructions.

**RT-qPCR.** mRNA was isolated from brown adipocytes using Trizol (ThermoFischer Scientific, Waltham, USA). Reverse transcription was performed with ProtoScript® II First Strand cDNA Synthesis Kit (New England Biolabs, Ipswitch, USA). qPCR was performed with Power SYBR™ Green PCR Master Mix (ThermoFischer Scientific, Waltham, USA).

**Data availability.** The raw data that support the findings of this study are available from the corresponding author upon reasonable request.

ASSOCIATED CONTENT

**Supporting Information**.

The following files include all supplementary figures as well as all MPI and MRI parameters, and are available free of charge at the ACS Publications website.

Supplementary figures (PDF)

Detailed lists of MPI and MRI reconstruction and imaging parameters (PDF)

AUTHOR INFORMATION

**Corresponding Author**

*E-mail: alexander.pfeifer@uni-bonn.de

REFERENCES

1.    Pfeifer, A. and Hoffmann, L. S. Brown, Beige, and White: The New Color Code of Fat and Its Pharmacological Implications. *Annu. Rev. Pharmacol. Toxicol.* **2015**, 55(207-27

2.    Kajimura, S.; Spiegelman, B. M.; Seale, P. Brown and Beige Fat: Physiological Roles Beyond Heat Generation. *Cell Metab.* **2015**, 22(4), 546-59

3.    Rosenwald, M. and Wolfrum, C. The Origin and Definition of Brite *Versus* White and Classical Brown Adipocytes. *Adipocyte* **2014**, 3(1), 4-9

4.    Cypess, A. M.; Lehman, S.; Williams, G.; Tal, I.; Rodman, D.; Goldfine, A. B.; Kuo, F. C.; Palmer, E. L.; Tseng, Y. H.; Doria, A.; Kolodny, G. M.; Kahn, C. R. Identification and Importance of Brown Adipose Tissue in Adult Humans. *N. Engl. J. Med.* **2009**, 360(15), 1509-17

5.    Nedergaard, J.; Bengtsson, T.; Cannon, B. Unexpected Evidence for Active Brown Adipose Tissue in Adult Humans. *Am. J. Physiol. Endocrinol. Metab.* **2007**, 293(2), E444-52

6.    Saito, M.; Okamatsu-Ogura, Y.; Matsushita, M.; Watanabe, K.; Yoneshiro, T.; Nio-Kobayashi, J.; Iwanaga, T.; Miyagawa, M.; Kameya, T.; Nakada, K.; Kawai, Y.; Tsujisaki, M. High Incidence of Metabolically Active Brown Adipose Tissue in Healthy Adult Humans: Effects of Cold Exposure and Adiposity. *Diabetes* **2009**, 58(7), 1526-31

7.  van Marken Lichtenbelt, W. D.; Vanhommerig, J. W.; Smulders, N. M.; Drossaerts, J. M.; Kemerink, G. J.; Bouvy, N. D.; Schrauwen, P.; Teule, G. J. Cold-Activated Brown Adipose Tissue in Healthy Men. *N. Engl. J. Med.* **2009**, 360(15), 1500-8

8.  Virtanen, K. A.; Lidell, M. E.; Orava, J.; Heglind, M.; Westergren, R.; Niemi, T.; Taittonen, M.; Laine, J.; Savisto, N. J.; Enerback, S.; Nuutila, P. Functional Brown Adipose Tissue in Healthy Adults. *N. Engl. J. Med.* **2009**, 360(15), 1518-25

9.  Becher, T.; Palanisamy, S.; Kramer, D. J.; Marx, S. J.; Wibmer, A. G.; Del Gaudio, I.; Butler, S. D.; Jiang, C. S.; Vaughan, R.; Schöder, H.; Di Lorenzo, A.; Mark, A.; Cohen, P. Brown Adipose Tissue Is Associated with Improved Cardiometabolic Health and Regulates Blood Pressure. *bioRxiv* **2020**,

10. Nedergaard, J.; Bengtsson, T.; Cannon, B. Three Years with Adult Human Brown Adipose Tissue. *Ann. N. Y. Acad. Sci.* **2010**, 1212(E20-36

11. Seale, P. and Lazar, M. A. Brown Fat in Humans: Turning up the Heat on Obesity. *Diabetes* **2009**, 58(7), 1482-1484

12. Nedergaard, J.; Bengtsson, T.; Cannon, B. New Powers of Brown Fat: Fighting the Metabolic Syndrome. *Cell Metab.* **2011**, 13(3), 238-240

13. Bartelt, A.; Bruns, O. T.; Reimer, R.; Hohenberg, H.; Ittrich, H.; Peldschus, K.; Kaul, M. G.; Tromsdorf, U. I.; Weller, H.; Waurisch, C.; Eychmuller, A.; Gordts, P. L. S. M.; Rinninger, F.; Bruegelmann, K.; Freund, B.; Nielsen, P.; Merkel, M.; Heeren, J. Brown Adipose Tissue Activity Controls Triglyceride Clearance. *Nat. Med.* **2011**, 17(2), 200-U93

14. Khedoe, P. P. S. J.; Hoeke, G.; Kooijman, S.; Dijk, W.; Buijs, J. T.; Kersten, S.; Havekes, L. M.; Hiemstra, P. S.; Berbee, J. F. P.; Boon, M. R.; Rensen, P. C. N. Brown Adipose Tissue Takes up Plasma Triglycerides Mostly after Lipolysis. *J. Lipid Res.* **2015**, 56(1), 51-59

15. Ouellet, V.; Labbe, S. M.; Blondin, D. P.; Phoenix, S.; Guerin, B.; Haman, F.; Turcotte, E. E.; Richard, D.; Carpentier, A. C. Brown Adipose Tissue Oxidative Metabolism Contributes to Energy Expenditure During Acute Cold Exposure in Humans. *J. Clin. Invest.* **2012**, 122(2), 545-552

16. Townsend, K. L. and Tseng, Y. H. Brown Fat Fuel Utilization and Thermogenesis. *Trends Endocrinol. Metab.* **2014**, 25(4), 168-77

17. Dominiczak, M. H. and Caslake, M. J. Apolipoproteins: Metabolic Role and Clinical Biochemistry Applications. *Ann. Clin. Biochem.* **2011**, 48(Pt 6), 498-515

18. Mahley, R. W.; Innerarity, T. L.; Rall, S. C., Jr.; Weisgraber, K. H. Plasma Lipoproteins: Apolipoprotein Structure and Function. *J. Lipid Res.* **1984**, 25(12), 1277-94

19. Casley-Smith, J. R. The Identification of Chylomicra and Lipoproteins in Tissue Sections and Their Passage into Jejunal Lacteals. *J. Cell Biol.* **1962**, 15(259-77

20. Berbee, J. F. P.; Boon, M. R.; Khedoe, P. P. S. J.; Bartelt, A.; Schlein, C.; Worthmann, A.; Kooijman, S.; Hoeke, G.; Mol, I. M.; John, C.; Jung, C.; Vazirpanah, N.; Brouwers, L. P. J.; Gordts, P. L. S. M.; Esko, J. D.; Hiemstra, P. S.; Havekes, L. M.; Scheja, L.; Heeren, J.; Rensen, P. C. N. Brown Fat Activation Reduces Hypercholesterolaemia and Protects from Atherosclerosis Development. *Nat Commun* **2015**, 6(

21. Mulder, W. J. M.; van Leent, M. M. T.; Lameijer, M.; Fisher, E. A.; Fayad, Z. A.; Perez-Medina, C. High-Density Lipoprotein Nanobiologics for Precision Medicine. *Acc. Chem. Res.* **2018**, 51(1), 127-137

22.  Giammanco, A.; Cefalu, A. B.; Noto, D.; Averna, M. R. The Pathophysiology of Intestinal Lipoprotein Production. *Front. Physiol.* **2015**, 6(61

23.  Goudriaan, J. R.; den Boer, M. A. M.; Rensen, P. C. N.; Febbraio, M.; Kuipers, F.; Romijn, J. A.; Havekes, L. M.; Voshol, P. J. Cd36 Deficiency in Mice Impairs Lipoprotein Lipase-Mediated Triglyceride Clearance. *J. Lipid Res.* **2005**, 46(10), 2175-2181

24.  Huang, B.; Law, M. W.; Khong, P. L. Whole-Body Pet/Ct Scanning: Estimation of Radiation Dose and Cancer Risk. *Radiology* **2009**, 251(1), 166-74

25.  Blondin, D. P.; Labbe, S. M.; Noll, C.; Kunach, M.; Phoenix, S.; Guerin, B.; Turcotte, E. E.; Haman, F.; Richard, D.; Carpentier, A. C. Selective Impairment of Glucose but Not Fatty Acid or Oxidative Metabolism in Brown Adipose Tissue of Subjects with Type 2 Diabetes. *Diabetes* **2015**, 64(7), 2388-97

26.  van Rooijen, B. D.; van der Lans, A. A.; Brans, B.; Wildberger, J. E.; Mottaghy, F. M.; Schrauwen, P.; Backes, W. H.; van Marken Lichtenbelt, W. D. Imaging Cold-Activated Brown Adipose Tissue Using Dynamic T2*-Weighted Magnetic Resonance Imaging and 2-Deoxy-2-[18f]Fluoro-D-Glucose Positron Emission Tomography. *Invest. Radiol.* **2013**, 48(10), 708-14

27.  Bruns, O. T.; Ittrich, H.; Peldschus, K.; Kaul, M. G.; Tromsdorf, U. I.; Lauterwasser, J.; Nikolic, M. S.; Mollwitz, B.; Merkel, M.; Bigall, N. C.; Sapra, S.; Reimer, R.; Hohenberg, H.; Weller, H.; Eychmuller, A.; Adam, G.; Beisiegel, U.; Heeren, J. Real-Time Magnetic Resonance Imaging and Quantification of Lipoprotein Metabolism *in Vivo* Using Nanocrystals. *Nat Nanotechnol* **2009**, 4(3), 193-201

28.  Baron, D. M.; Clerte, M.; Brouckaert, P.; Raher, M. J.; Flynn, A. W.; Zhang, H.; Carter, E. A.; Picard, M. H.; Bloch, K. D.; Buys, E. S.; Scherrer-Crosbie, M. *In Vivo* Noninvasive Characterization of Brown Adipose Tissue Blood Flow by Contrast Ultrasound in Mice. *Circ. Cardiovasc. Imaging* **2012**, 5(5), 652-9

29.  Riis-Vestergaard, M. J.; Breining, P.; Pedersen, S. B.; Laustsen, C.; Stodkilde-Jorgensen, H.; Borghammer, P.; Jessen, N.; Richelsen, B. Evaluation of Active Brown Adipose Tissue by the Use of Hyperpolarized [1-(13)C]Pyruvate Mri in Mice. *Int. J. Mol. Sci.* **2018**, 19(9),

30.  Biederer, S.; Knopp, T.; Sattel, T. F.; Ludtke-Buzug, K.; Gleich, B.; Weizenecker, J.; Borgert, J.; Buzug, T. M. Magnetization Response Spectroscopy of Superparamagnetic Nanoparticles for Magnetic Particle Imaging. *J Phys D Appl Phys* **2009**, 42(20),

31.  Gleich, B. and Weizenecker, R. Tomographic Imaging Using the Nonlinear Response of Magnetic Particles. *Nature* **2005**, 435(7046), 1214-1217

32.  Tay, Z. W.; Chandrasekharan, P.; Zhou, X. Y.; Yu, E.; Zheng, B.; Conolly, S. *In Vivo* Tracking and Quantification of Inhaled Aerosol Using Magnetic Particle Imaging Towards Inhaled Therapeutic Monitoring. *Theranostics* **2018**, 8(13), 3676-3687

33.  Paysen, H.; Loewa, N.; Weber, K.; Kosch, O.; Wells, J.; Schaeffter, T.; Wiekhorst, F. Imaging and Quantification of Magnetic Nanoparticles: Comparison of Magnetic Resonance Imaging and Magnetic Particle Imaging. *J. Magn. Magn. Mater.* **2019**, 475(382-388

34.  Bauer, L. M.; Situ, S. F.; Griswold, M. A.; Samia, A. C. High-Performance Iron Oxide Nanoparticles for Magnetic Particle Imaging - Guided Hyperthermia (Hmpi). *Nanoscale* **2016**, 8(24), 12162-9

35. Tay, Z. W.; Chandrasekharan, P.; Chiu-Lam, A.; Hensley, D. W.; Dhavalikar, R.; Zhou, X. Y.; Yu, E. Y.; Goodwill, P. W.; Zheng, B.; Rinaldi, C.; Conolly, S. M. Magnetic Particle Imaging-Guided Heating *in Vivo* Using Gradient Fields for Arbitrary Localization of Magnetic Hyperthermia Therapy. *ACS Nano* **2018**, 12(4), 3699-3713

36. Ludewig, P.; Gdaniec, N.; Sedlacik, J.; Forkert, N. D.; Szwargulski, P.; Graeser, M.; Adam, G.; Kaul, M. G.; Krishnan, K. M.; Ferguson, R. M.; Khandhar, A. P.; Walczak, P.; Fiehler, J.; Thomalla, G.; Gerloff, C.; Knopp, T.; Magnus, T. Magnetic Particle Imaging for Real-Time Perfusion Imaging in Acute Stroke. *Acs Nano* **2017**, 11(10), 10480-10488

37. Yu, E. Y.; Chandrasekharan, P.; Berzon, R.; Tay, Z. W.; Zhou, X. Y. Y.; Khandhar, A. P.; Ferguson, R. M.; Kemp, S. J.; Zheng, B.; Goodwill, P. W.; Wendland, M. F.; Krishnan, K. M.; Behr, S.; Carter, J.; Conolly, S. M. Magnetic Particle Imaging for Highly Sensitive, Quantitative, and Safe *in Vivo* Gut Bleed Detection in a Murine Model. *Acs Nano* **2017**, 11(12), 12067-12076

38. Zheng, B.; von See, M. P.; Yu, E.; Gunel, B.; Lu, K.; Vazin, T.; Schaffer, D. V.; Goodwill, P. W.; Conolly, S. M. Quantitative Magnetic Particle Imaging Monitors the Transplantation, Biodistribution, and Clearance of Stem Cells *in Vivo*. *Theranostics* **2016**, 6(3), 291-301

39. Krycka, K. L.; Booth, R. A.; Hogg, C. R.; Ijiri, Y.; Borchers, J. A.; Chen, W. C.; Watson, S. M.; Laver, M.; Gentile, T. R.; Dedon, L. R.; Harris, S.; Rhyne, J. J.; Majetich, S. A. Core-Shell Magnetic Morphology of Structurally Uniform Magnetite Nanoparticles. *Phys. Rev. Lett.* **2010**, 104(20), 207203

40. Unni, M.; Uhl, A. M.; Savliwala, S.; Savitzky, B. H.; Dhavalikar, R.; Garraud, N.; Arnold, D. P.; Kourkoutis, L. F.; Andrew, J. S.; Rinaldi, C. Thermal Decomposition Synthesis of Iron Oxide Nanoparticles with Diminished Magnetic Dead Layer by Controlled Addition of Oxygen. *ACS Nano* **2017**, 11(2), 2284-2303

41. Kratz, H.; Taupitz, M.; Ariza de Schellenberger, A.; Kosch, O.; Eberbeck, D.; Wagner, S.; Trahms, L.; Hamm, B.; Schnorr, J. Novel Magnetic Multicore Nanoparticles Designed for Mpi and Other Biomedical Applications: From Synthesis to First *in Vivo* Studies. *PLoS One* **2018**, 13(1), e0190214

42. van Dam, A. D.; Nahon, K. J.; Kooijman, S.; van den Berg, S. M.; Kanhai, A. A.; Kikuchi, T.; Heemskerk, M. M.; van Harmelen, V.; Lombes, M.; van den Hoek, A. M.; de Winther, M. P.; Lutgens, E.; Guigas, B.; Rensen, P. C.; Boon, M. R. Salsalate Activates Brown Adipose Tissue in Mice. *Diabetes* **2015**, 64(5), 1544-54

43. Liu, D.; Bordicchia, M.; Zhang, C.; Fang, H.; Wei, W.; Li, J. L.; Guilherme, A.; Guntur, K.; Czech, M. P.; Collins, S. Activation of Mtorc1 Is Essential for Beta-Adrenergic Stimulation of Adipose Browning. *J. Clin. Invest.* **2016**, 126(5), 1704-16

44. Harms, M. and Seale, P. Brown and Beige Fat: Development, Function and Therapeutic Potential. *Nat. Med.* **2013**, 19(10), 1252-63

45. Blondin, D. P.; Tingelstad, H. C.; Noll, C.; Frisch, F.; Phoenix, S.; Guerin, B.; Turcotte, E. E.; Richard, D.; Haman, F.; Carpentier, A. C. Dietary Fatty Acid Metabolism of Brown Adipose Tissue in Cold-Acclimated Men. *Nat Commun* **2017**, 8(14146

46. Haman, F.; Peronnet, F.; Kenny, G. P.; Massicotte, D.; Lavoie, C.; Weber, J. M. Partitioning Oxidative Fuels During Cold Exposure in Humans: Muscle Glycogen Becomes Dominant as Shivering Intensifies. *J Physiol-London* **2005**, 566(1), 247-256

47. Fitzgibbons, T. P.; Kogan, S.; Aouadi, M.; Hendricks, G. M.; Straubhaar, J.; Czech, M. P. Similarity of Mouse Perivascular and Brown Adipose Tissues and Their Resistance to Diet-Induced Inflammation. *Am J Physiol-Heart C* **2011**, 301(4), H1425-H1437

48. Chang, L.; Villacorta, L.; Li, R. X.; Hamblin, M.; Xu, W.; Dou, C. Y.; Zhang, J. F.; Wu, J. R.; Zeng, R.; Chen, Y. E. Loss of Perivascular Adipose Tissue on Peroxisome Proliferator-Activated Receptor-Gamma Deletion in Smooth Muscle Cells Impairs Intravascular Thermoregulation and Enhances Atherosclerosis. *Circulation* **2012**, 126(9), 1067-U174

49. Szczerba, W.; Zukrowski, J.; Przybylski, M.; Sikora, M.; Safonova, O.; Shmeliov, A.; Nicolosi, V.; Schneider, M.; Granath, T.; Oppmann, M.; Strasser, M.; Mandel, K. Pushing up the Magnetisation Values for Iron Oxide Nanoparticles *Via* Zinc Doping: X-Ray Studies on the Particle's Sub-Nano Structure of Different Synthesis Routes. *Phys. Chem. Chem. Phys.* **2016**, 18(36), 25221-25229

50. Vakili-Ghartavol, R.; Momtazi-Borojeni, A. A.; Vakili-Ghartavol, Z.; Aiyelabegan, H. T.; Jaafari, M. R.; Rezayat, S. M.; Arbabi Bidgoli, S. Toxicity Assessment of Superparamagnetic Iron Oxide Nanoparticles in Different Tissues. *Artif Cells Nanomed Biotechnol* **2020**, 48(1), 443-451

51. Plum, L. M.; Rink, L.; Haase, H. The Essential Toxin: Impact of Zinc on Human Health. *Int. J. Environ. Res. Public Health* **2010**, 7(4), 1342-65

52. Zhu, S.; Xu, X.; Rong, R.; Li, B.; Wang, X. Evaluation of Zinc-Doped Magnetite Nanoparticle Toxicity in the Liver and Kidney of Mice after Sub-Chronic Intragastric Administration. *Toxicol Res (Camb)* **2016**, 5(1), 97-106

53. Lee, J.; Yu, W. J.; Song, J.; Sung, C.; Jeong, E. J.; Han, J. S.; Kim, P.; Jo, E.; Eom, I.; Kim, H. M.; Kwon, J. T.; Choi, K.; Choi, J.; Kim, H.; Lee, H.; Park, J.; Jin, S. M.; Park, K. Developmental Toxicity of Intravenously Injected Zinc Oxide Nanoparticles in Rats. *Arch. Pharm. Res.* **2016**, 39(12), 1682-1692

54. Geiser, J.; Venken, K. J.; De Lisle, R. C.; Andrews, G. K. A Mouse Model of Acrodermatitis Enteropathica: Loss of Intestine Zinc Transporter Zip4 (Slc39a4) Disrupts the Stem Cell Niche and Intestine Integrity. *PLoS Genet.* **2012**, 8(6), e1002766

55. Galvez-Peralta, M.; He, L.; Jorge-Nebert, L. F.; Wang, B.; Miller, M. L.; Eppert, B. L.; Afton, S.; Nebert, D. W. Zip8 Zinc Transporter: Indispensable Role for Both Multiple-Organ Organogenesis and Hematopoiesis in Utero. *PLoS One* **2012**, 7(5), e36055

56. Weber, A.; Werner, F.; Weizenecker, J.; Buzug, T. M.; Knopp, T. Artifact Free Reconstruction with the System Matrix Approach by Overscanning the Field-Free-Point Trajectory in Magnetic Particle Imaging. *Phys. Med. Biol.* **2016**, 61(2), 475-87

57. Knopp, T.; Them, K.; Kaul, M.; Gdaniec, N. Joint Reconstruction of Non-Overlapping Magnetic Particle Imaging Focus-Field Data. *Phys. Med. Biol.* **2015**, 60(8), L15-21

58. Chandrasekharan, P.; Tay, Z. W.; Zhou, X. Y.; Yu, E.; Orendorff, R.; Hensley, D.; Huynh, Q.; Fung, K. L. B.; VanHook, C. C.; Goodwill, P.; Zheng, B.; Conolly, S. A Perspective on a Rapid and Radiation-Free Tracer Imaging Modality, Magnetic Particle Imaging, with Promise for Clinical Translation. *Br. J. Radiol.* **2018**, 91(1091), 20180326

59. Tay, Z. W.; Hensley, D. W.; Chandrasekharan, P.; Zheng, B.; Conolly, S. M. Optimization of Drive Parameters for Resolution, Sensitivity and Safety in Magnetic Particle Imaging. *IEEE Trans. Med. Imaging* **2020**, 39(5), 1724-1734

60. Graeser, M.; Thieben, F.; Szwargulski, P.; Werner, F.; Gdaniec, N.; Boberg, M.; Griese, F.; Moddel, M.; Ludewig, P.; van de Ven, D.; Weber, O. M.; Woywode, O.; Gleich, B.;

Knopp, T. Human-Sized Magnetic Particle Imaging for Brain Applications. *Nat Commun* **2019**, 10(1), 1936

61.     Carneiro, M. M.; Miname, M. H.; Gagliardi, A. C.; Pereira, C.; Pereira, A. C.; Krieger, J. E.; Maranhao, R. C.; Santos, R. D. The Removal from Plasma of Chylomicrons and Remnants Is Reduced in Heterozygous Familial Hypercholesterolemia Subjects with Identified Ldl Receptor Mutations: Study with Artificial Emulsions. *Atherosclerosis* **2012**, 221(1), 268-274

62.     Meyer, J. M.; Ji, A.; Cai, L.; van der Westhuyzen, D. R. High-Capacity Selective Uptake of Cholesteryl Ester from Native Ldl During Macrophage Foam Cell Formation. *J. Lipid Res.* **2012**, 53(10), 2081-91

63.     Shadid, S.; Koutsari, C.; Jensen, M. D. Direct Free Fatty Acid Uptake into Human Adipocytes *in Vivo*: Relation to Body Fat Distribution. *Diabetes* **2007**, 56(5), 1369-75

64.     Hachani, R.; Lowdell, M.; Birchall, M.; Hervault, A.; Mertz, D.; Begin-Coline, S.; Thanh, N. T. K. Polyol Synthesis, Functionalisation, and Biocompatibility Studies of Superparamagnetic Iron Oxide Nanoparticles as Potential Mri Contrast Agents. *Nanoscale* **2016**, 8(6), 3278-3287

65.     Loewa, N.; Wiekhorst, F.; Gemeinhardt, I.; Ebert, M.; Schnorr, J.; Wagner, S.; Taupitz, M.; Trahms, L. Cellular Uptake of Magnetic Nanoparticles Quantified by Magnetic Particle Spectroscopy. *IEEE Transactions on Magnetics* **2013**, 49(1), 275-278

66.     Poller, W. C.; Lowa, N.; Wiekhorst, F.; Taupitz, M.; Wagner, S.; Moller, K.; Baumann, G.; Stangl, V.; Trahms, L.; Ludwig, A. Magnetic Particle Spectroscopy Reveals Dynamic Changes in the Magnetic Behavior of Very Small Superparamagnetic Iron Oxide Nanoparticles During Cellular Uptake and Enables Determination of Cell-Labeling Efficacy. *J. Biomed. Nanotechnol.* **2016**, 12(2), 337-46

67.     Löwa, N.; Seidel, M.; Radon, P.; Wiekhorst, F. Magnetic Nanoparticles in Different Biological Environments Analyzed by Magnetic Particle Spectroscopy. *J. Magn. Magn. Mater.* **2017**, 427(133-138

68.     Paysen, H.; Wells, J.; Kosch, O.; Steinhoff, U.; Franke, J.; Trahms, L.; Schaeffter, T.; Wiekhorst, F. Improved Sensitivity and Limit-of-Detection Using a Receive-Only Coil in Magnetic Particle Imaging. *Phys. Med. Biol.* **2018**, 63(13),

69.     Rahmer, J.; Weizenecker, J.; Gleich, B.; Borgert, J. Signal Encoding in Magnetic Particle Imaging: Properties of the System Function. *BMC Med. Imaging* **2009**, 9(4

70.     Rahmer, J.; Weizenecker, J.; Gleich, B.; Borgert, J. Analysis of a 3-D System Function Measured for Magnetic Particle Imaging. *IEEE Trans. Med. Imaging* **2012**, 31(6), 1289-99

71.     Marks, G.; Steinhoff, U.; Wiekhorst, F. A Model for Uncertainty Influences on Static Magnetisation Measurements on Magnetic Nanoparticles. *Journal of Physics: Conference Series* **2018**, 1065(072030

72.     Ludwig, A.; Poller, W. C.; Westphal, K.; Minkwitz, S.; Lattig-Tunnemann, G.; Metzkow, S.; Stangl, K.; Baumann, G.; Taupitz, M.; Wagner, S.; Schnorr, J.; Stangl, V. Rapid Binding of Electrostatically Stabilized Iron Oxide Nanoparticles to Thp-1 Monocytic Cells *Via* Interaction with Glycosaminoglycans. *Basic Res. Cardiol.* **2013**, 108(2),

73.     Chantrell, R.; Popplewell, J.; Charles, S. Measurements of Particle Size Distribution Parameters in Ferrofluids. *IEEE Transactions on Magnetics* **1978**, 14(5), 975-977

74.     Haas, B.; Mayer, P.; Jennissen, K.; Scholz, D.; Berriel Diaz, M.; Bloch, W.; Herzig, S.; Fassler, R.; Pfeifer, A. Protein Kinase G Controls Brown Fat Cell Differentiation and Mitochondrial Biogenesis. *Sci Signal* **2009**, 2(99), ra78